applied sciences

MDPI

Article

A Probabilistic Framework for the Robust Stability and Performance Analysis of Grid-Tied Voltage Source Converters

Hosein Gholami-Khesht, Pooya Davari *, Mateja Novak and Frede Blaabjerg

AAU Energy, Aalborg University, 9220 Aalborg, Denmark; hgk@energy.aau.dk (H.G.-K.); nov@energy.aau.dk (M.N.); fbl@energy.aau.dk (F.B.)
* Correspondence: pda@energy.aau.dk

Abstract: This paper proposed a probabilistic framework that could be used for the sensitivity assessment of grid-connected voltage source converters (VSCs), where uncertainties in the grid short circuit ratio (SCR) and operating point conditions, as well as control-loop interactions, were considered. The proposed method tried to broaden the available knowledge on the small-signal stability analysis of VSCs and provide a probabilistic point of view of this subject. It considered the probability of different operational conditions in order to obtain less conservatism and more accurate results. Based on uncertain inputs and the employed stability model, the proposed model produced statistical distributions of the critical mode and its damping factor and ratio, which were not accessible by existing deterministic methods. Crucial statistical information measures how much system stability and performance are maintained or changed over the system uncertainties and disturbances, as well as provides a clear insight into the system stability problem. For instance, as concluded in this paper, for the conventional control system design, fast dynamic parts of a VSC, such as the current controller and control delay, significantly impact the minimum damping ratio. Furthermore, slow dynamic parts, such as outer voltage control loops and the synchronization block, influence the maximum damping factor. For strong grids, the AC voltage magnitude controller (AVC) significantly impacts the maximum damping factor due to its lower bandwidth among all control loops. For weak grids, the damping factor of the critical mode is highly affected by interactions between the VSC, the power grid, and different control loops due to the synchronization mechanism. The other contributions of this paper were the introduction of robust stability and performance definitions and indices; explanations of the pros and cons of probabilistic assessment methods and their applicability; interpretation of the obtained results; and, finally, a link was provided between system stability and reliability, which will be crucial for future power system design.

Keywords: voltage source converters (VSCs); grid-connected VSC; weak grids; probabilistic stability analysis; Monte Carlo simulations; robustness analysis

Citation: Gholami-Khesht, H.; Davari, P.; Novak, M.; Blaabjerg, F. A Probabilistic Framework for the Robust Stability and Performance Analysis of Grid-Tied Voltage Source Converters. *Appl. Sci.* **2022**, *12*, 7375. https://doi.org/10.3390/app12157375

Academic Editor: Giovanni Petrone

Received: 5 July 2022
Accepted: 20 July 2022
Published: 22 July 2022

1. Introduction

Nowadays, methods of renewable energy generation, such as solar farms and wind power plants, have become an important part of the energy sector due to global climate change and the depletion of fossil fuel-based energy. It is worth noting that, by the end of 2020, the share of renewables in electricity generation was 27%, which is expected to reach 33% by 2025 [1]; however, these sources produce electrical energy that is inconsistent with power grid characteristics. Consequently, a power electronic converter is required to successfully transfer the electricity generated from these energy sources to the power grid, which results in highly aggregated modern power systems with many static power converters.

This rapid growth in power electronic systems has attracted considerable attention and concern from power system researchers and engineers, especially regarding the robust and reliable operation of these reformed systems due to their fast dynamics, wide timescale

control dynamics, and the interactions between different control loops, converters, and grids [2–7]. In addition to the mentioned issues, PEPS are subjected to various uncertainties and disturbances. Power system conditions change substantially during the day due to variations in the number and characteristics of connected generators and loads, equipment failure, and nonlinear effects of power converters. These issues make the robustness analysis of PEPS more challenging as their presence is increasing.

1.1. State of the Art

1.1.1. Nominal Stability Analysis

So far, many research works have been conducted for the small signal stability analysis of PEPS, either using the eigenvalue method or the impedance-based method.

Eigenvalue analysis clarifies essential information such as stable, unstable, and oscillation modes and participation factors of each system variable on the system modes. However, eigenvalue analysis is based on the system state–space representation and needs complete system information, which may not be available due to confidentiality rules of different vendors [8–12].

In the impedance-based method, the power system can be divided into two separate parts: a load-equivalent part and a source-equivalent part. The system stability can then be analyzed by the impedance ratio of the load and the source using the Nyquist criterion. This method needs less information about the system and analyzes system stability at the point of connection of each inverter. However, this method is unable to identify oscillation modes and participation factors of each system state [13–18].

These methods are popular due to the effectiveness and simplicity of their application. However, they have been developed for linear time-invariant (LTI) systems around a certain steady-state operating point. Therefore, they cannot investigate the impact of multiple uncertain parameters and operational point changes on the system's stability and performance. Eventually, without properly incorporating these potential system uncertainties, the stability assessment may lead to conservative or even inaccurate results.

1.1.2. Analytical Robust Stability Analysis

Recently, many efforts have been made to present advanced robust stability analysis methods for compensating for imperfections in the classical techniques. The most important methods are μ-analysis [19–21], the edge theorem [22], the Lyapunov function, and linear matrix inequality (LMI)-based approaches [23–25]. A structured singular value or μ-analysis is employed to assess the robust stability of an LCL grid-connected synchronverter where uncertainties in control parameters and grid conditions are modeled as unstructured (nonparametric) uncertainties [19]. In this paper, results have confirmed that μ-analysis could identify some effects, which might be unclear when performing an eigenvalue analysis. Moreover, μ-analysis concluded that the robustness of the synchronverter would be increased under weaker grid conditions (i.e., a grid with higher impedance), which was exactly opposite to the supposed results from eigenvalue analysis [26]. In [22], the stability robustness of a power system with participating wind power plants in the automatic generation control (AGC) task was analyzed by the edge theorem. In contrast to conventional units, the share of wind power systems was uncertain (but bounded), which limited the application of classical robustness analysis methods. The stability analysis of DC microgrids with uncertain constant power loads (CPLs) was investigated in [23,24]. An uncertain system was modeled as a linear system with polytopic uncertainties on system matrices in this work. Moreover, robustness analysis was performed using the Lyapunov stability theorem combined with the linear matrix inequalities (LMIs).

These robust stability-analysis methods are interesting and manifest different operational aspects of emerging power electronic-based power systems; however, they are mathematically complex and a high level of expertise is required to apply them. In addition, their application to a larger scale system with multiple uncertainties and disturbances is not easy at all. Moreover, these methods usually consider a system's worst-case scenario,

which might have an extremely low occurrence. Therefore, a power system design based on the obtained results might not be cost-effective and efficient. To better utilize existing assets, and at the same time properly incorporate all system uncertainties and disturbances in the stability analysis, probabilistic stability analysis could be considered as a simple and powerful tool [27–34].

1.1.3. Probabilistic Robust Stability Analysis

In probabilistic assessment, proper probability density functions (PDFs) for system uncertainties, operating point conditions, and the stochastic nature of renewable energy sources are defined. A sampling approach, such as the Monte Carlo (MC) sampling method, draws data from PDFs. Finally, sampled data are used in the stability model to determine statistical measures of the stability indicators.

Probabilistic stability analysis can provide more accurate results due to the examination of various influential parameters and their probability of occurrence. It can reveal the sensitivity of system outputs to the uncertainties and variations in the system inputs. Furthermore, in contrast to previous methods, probabilistic stability assessment can provide a much clearer picture of the system understudy and its behavior, and can facilitate appropriate actions to utilize it better, as summarized in Table 1 and compared to the state-of-the-art nominal and robust stability-analysis methods.

Table 1. State-of-the-art nominal and robust stability-analysis methods.

Methods	Nominal Stability	Robust Stability	Mathematical Complexity	Computational Burden	Conservatism	Link to Other Power System Studies
Conventional nominal stability analysis, e.g., eigenvalues analysis, Nyquist method, etc., [8–18]	Yes	No	Low	Low	Low	Hard
Analytical robust stability-analysis methods, e.g., μ-analysis [19–25]	Yes	Yes	High	Medium	High	Hard
Probabilistic robust stability analysis [31–34]	Yes	Yes	Medium	High	Low	Easy

However, so far, probabilistic assessment has not been widely used in modern power system studies except for specific topics, such as reliability assessment (adequacy and security) [35–37], lifetime estimation [38], and efficiency calculation [39]. In [31–34], probabilistic-transient and small-signal stability assessments have been performed in order to consider the impact of load variations, the stochastic generation of renewable energy sources, and other system disturbances. However, stability analysis is based on rotor-angle stability analysis that was developed for low-frequency stability analysis of traditional power systems. It cannot clarify different mentioned challenges in PEPS, such as wide timescale control dynamics and interactions between other control loops and the power grid.

1.2. Paper Motivations and Contributions

This paper helped to develop a comprehensive probabilistic framework for PEPS that could reflect changes in the overall dynamic behavior of a system under different uncertainties and disturbances.

In this respect, the primary motivations and contributions of this work were as follows:

- A workflow diagram for probabilistic robust stability and performance analysis was proposed; it was helpful to be able to better understand how the probabilistic robustness assessment was implemented and how different calculation parts were related.
- Various features of the probabilistic robustness assessment were clarified; this paper presented how probabilistic assessment could be used for small-signal analysis meth-

ods of PEPS, how obtained results could be interpreted, and what their advantages and disadvantages were.

- Nominal and robust stability and performance definitions and indices were provided; this paper tried to clarify nominal stability and performance, robust stability, and performance and how they could be calculated based on the critical mode and damping factor and ratio.
- A link between system stability and the risk and reliability assessment was provided and the probabilistic assessment methods could provide PDFs and CDFs of stability indices; therefore, they could provide the probability of a specific condition or a system's stability and instability. This information could be used for a further power system reliability assessment.
- Major contributing parameters to system stability and performance (parameters or control loops with a more significant impact on the maximum damping factor and minimum damping ratio) were found.

1.3. Paper Structure

The remainder of this paper is organized as follows. Section 2 presents the proposed framework for probabilistic stability and performance assessment and employed system operational indicators. The system that was studied, a grid-connected LCL-filtered voltage source converter (VSC), which included all inner and outer control loops, is introduced in Section 3. The small-signal modeling of the power system and operating point calculations are then discussed. After that, the application of the proposed algorithm to probabilistic stability and the performance assessment of a grid-connected VSC is demonstrated in Section 4. This section investigates the impact of grid short circuit ratios (SCRs), different operating point conditions, and control parameters on the system stability and performance, and recommendations are made. Additionally, simulations and experiments have also been provided to validate the analytical conclusions in Sections 4 and 5. After that, a review and comprehensive discussion on the obtained results are presented, and future works are identified in Section 6. Finally, Section 7 concludes the paper.

2. Proposed Framework for Probabilistic Stability and Performance Assessment

The robustness assessment can be considered in two different levels: the converter level and the system level. This paper's primary goal was to present and discuss a systematic way to perform a probabilistic assessment at the converter level. A single grid-connected VSC was considered, and the impact of the power grid and operating point conditions and control-loop bandwidths were studied in relation to the system stability and performance. The proposed flow diagram for a probabilistic robustness assessment at the converter level is shown in Figure 1. A single VSC with known control parameters was connected to the power grid at PCC. It is worth remarking that the power grid was represented by a Thevenin equivalent model, and the grid SCR or grid equivalent inductance could vary over a wide range and it was unknown. Moreover, the inverter power level was dictated by the power profiles of the renewable sources or power flow calculations at the higher level. This might also have affected the system's stability and performance. In the proposed algorithm, at first, proper PDFs for uncertain parameters, such as grid SCR, were defined in order to consider its variations. A Monte Carlo sampling method was then employed to draw parameters from the PDFs. The sampled and fixed parameters were entered into the operating point calculation. After that, the stability model was built based on the available data and the linearized time-invariant state–space model. The eigenvalue analysis calculated the system's critical mode and its damping factor and ratio. This procedure was repeated N_C times for different sampled parameters that were provided by MC.

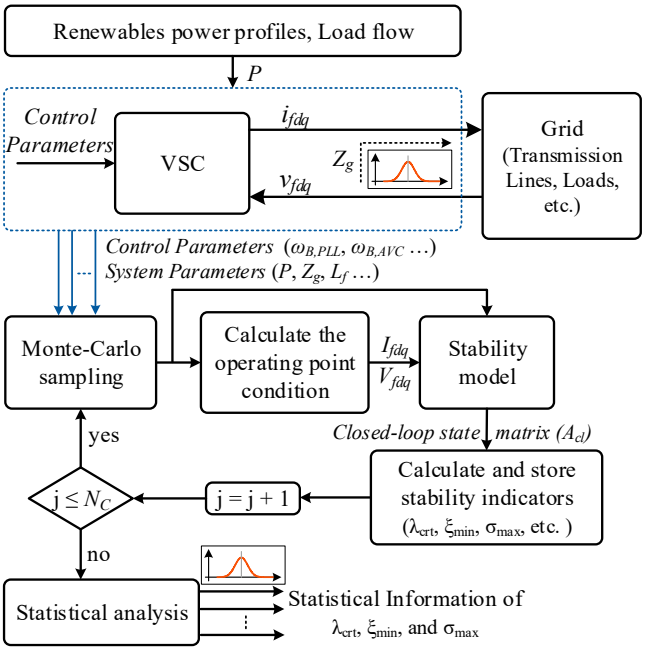

Figure 1. Proposed flow diagram for probabilistic stability and performance assessment of a grid-connected VSC.

Finally, the statistical characteristics of the outputs, which were of utmost importance, were computed and plotted.

2.1. Definitions, Stability and Performance Indicators

In a power electronic-based power system, the unstable or lightly damped modes caused significant oscillations or even system instability; therefore, identifying these modes, as well as the most influential parameters on them, was very important. The critical mode was an unstable eigenvalue or weakest damped eigenvalue among all the eigenvalues. Placing the critical mode to the left side of the s-plane can guarantee system stability and improve system performance.

The following complex equation can represent the eigenvalue of a system:

$$\lambda = \sigma \pm j\omega_d \tag{1}$$

The real part is the damping factor (σ) and shows the relative system stability. The imaginary part is called the damped frequency (ω_d) or frequency of oscillations. Another stability and performance indictor is the damping ratio (ξ), which measures the system performance in terms of overshoot:

$$\xi = \frac{-\sigma}{\sqrt{\sigma^2 + {\omega_d}^2}} \tag{2}$$

To have some stability margin, the damping factor of the critical mode should be less than a maximum value ($\sigma \leq \sigma_{\max}$). This places all closed-loop eigenvalues in a sector, as shown in Figure 2a. Moreover, to limit a system's overshoot, it is desirable to keep the worst damping ratio greater than a minimum value ($\xi \geq \xi_{\min}$), as shown in the wedge-shaped sector in Figure 2b. When both damping factor and damping ratio meet the required requirements simultaneously, the system closed-loop eigenvalues are placed in the D-shaped sector in which $\sigma \leq \sigma_{\max}$ and $\xi \geq \xi_{\min}$, as shown in Figure 2c.

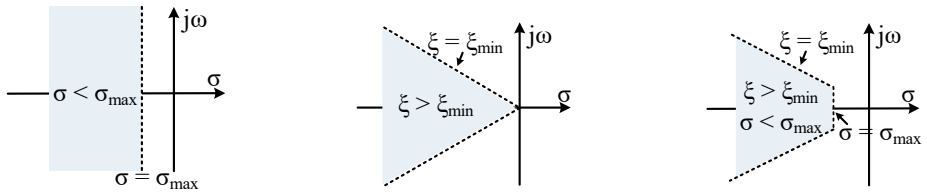

(**a**) (**b**) (**c**)

Figure 2. Region of eigenvalue location based on the different stability and performance objectives. (**a**) Region in the left-side of the s-plane where $\sigma < \sigma_{max}$; (**b**) a wedge-shaped sector in the s-plane where $\xi > \xi_{min}$; (**c**) a D-shaped sector in the s-plane where $\sigma < \sigma_{max}$ & $\xi > \xi_{min}$.

It is worth mentioning that the system was exponentially stable for $\sigma_{max} < 0$ and $\xi_{min} > 0$, and oscillating or unstable for $\sigma_{max} \geq 0$ and $\xi_{min} \leq 0$. Therefore, based on the imposed conditions on σ and ξ, and whether the system uncertainty was considered or not, four different definitions for the nominal and robust stability and performance could be defined as follows:

Nominal stability (NS): the closed-loop system was exponentially stable when the plant was known precisely, i.e.,

$$\begin{cases} \sigma < 0,\ \xi > 0 \\ \text{Uncertainties} = 0 \end{cases} \rightarrow \text{Nominal Stability analysis}$$

Robust stability (RS): the closed-loop system was exponentially stable when there were one or more uncertain parameters in the plant, i.e.,

$$\begin{cases} \sigma < 0,\ \xi > 0 \\ \text{Uncertainties} \neq 0 \end{cases} \rightarrow \text{Robust Stability analysis}$$

Nominal performance (NP): the closed-loop system met the performance specifications when the plant was known precisely, i.e.,

$$\begin{cases} \sigma_{min} \leq \sigma \leq \sigma_{max},\ \xi_{min} \leq \xi \leq \xi_{max} \\ \text{Uncertainties} = 0 \end{cases} \rightarrow \text{Nominal Performance analysis}$$

Robust Performance (RP): the closed-loop system met the performance specifications under system uncertainties, i.e.,

$$\begin{cases} \sigma_{min} \leq \sigma \leq \sigma_{max},\ \xi_{min} \leq \xi \leq \xi_{max} \\ \text{Uncertainties} \neq 0 \end{cases} \rightarrow \text{Robust Performance analysis}$$

2.2. The Stopping Criterion for Monte Carlo (MC) Simulations

Although increasing the amount of sampled data and MC simulations (N_C) resulted in a higher accuracy of the obtained results, it also increased the computational demands. Therefore, the selection of N_C was a compromise between the accuracy and computational burden. Accordingly, a stopping criterion was needed. Figure 3 shows the error of the estimated damping factor mean value under different iterations of MC simulation, which were associated with the ideal case (damping factor mean value under an approximately infinite number of iterations). Moreover, the time needed to conduct MC simulations for some cases is also depicted.

It could be seen that 2000 iterations were sufficient to provide a satisfactory result since the stability criteria surely had errors in a mean of less than 2% and the required time to carry out MC simulations was acceptable. The same conclusions could also be obtained for other stability and performance criteria and grid conditions, which were not presented here due to limited space.

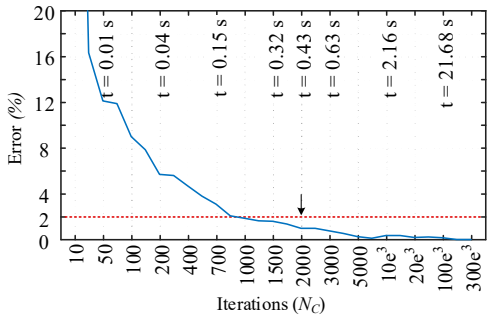

Figure 3. Stopping criterion for the maximum damping factor (SCR = 1.67, $P = P_n$).

3. Test System, Description, and Modeling

The proposed probabilistic framework could be applied to different PEPS. Among others, this work considered the most commonly used structure of LCL-filtered grid-connected VSCs, which revealed the most stability issues that were usually related to the low-frequency oscillations. This was due to lower SCR and PLL and high-frequency oscillations due to LCL-filter resonance and delay.

The principal scheme of the studied system is depicted in Figure 4. The main aim was to inject the power produced by renewables into the power grid and help the power system keep the voltage at the point of common coupling (PCC) within the allowable ranges. The power system included primary energy sources, the power grid, a three-phase voltage source converter (VSC), an LCL output filter, and a control system.

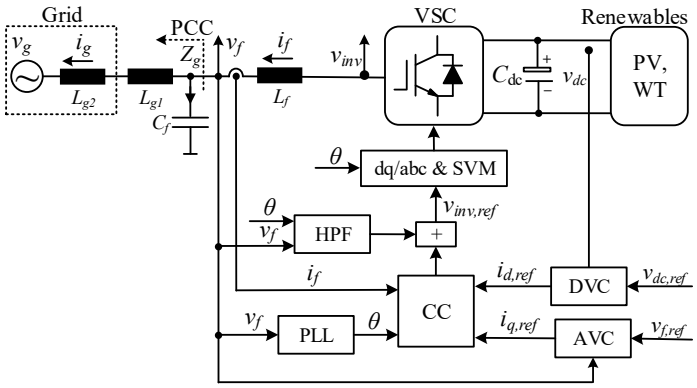

Figure 4. Single line diagram of a grid-connected three-phase voltage source converter (VSC).

The Thevenin model represented the power grid as seen from the PCC. Its impedance could also vary to emulate a weaker or stronger connection point. The control system consisted of five main parts, which included the DC-link voltage controller (DVC), AC voltage magnitude controller (AVC), current controller (CC), highpass filter (HPF), and synchronous reference frame phase-locked loop (SRF-PLL).

The DVC regulated the active power or DC-link voltage at the desired value, and the AVC controled the reactive power or PCC voltage magnitude. The outer voltage control loops generated the reference for the inner current control loop (CC), and CC provided inverter current control and protection. For PCC voltage synchronization, a PLL was also required. It is worth remarking that all of these employed a proportional-integral (PI) controller to ensure a good dynamic response and zero steady-state tracking errors in the synchronous reference frame. Finally, a voltage feedforward control-based HPF emulated a virtual resistor paralleled with the filter capacitor to dampen the LCL filter resonances. The remaining parameters in Figure 4 are as follows: i_f, i_g, v_f, v_{inv}, and v_{dc} are converter and grid currents, the voltage across the filter capacitor, inverter output voltage, and DC-link voltage, respectively. In addition, Z_g, L_f, L_{g1}, C_f, L_{g2}, and C_{dc} represent the seen impedance from PCC, the converter and grid-side filter inductances, filter capacitance, equivalent

grid inductance, and DC-link capacitance, respectively. Additionally, θ is the phase angle obtained by the PLL, and the subscript reference gives the reference values for different control loops.

3.1. Small-Signal Modeling of the Grid-Connected Three-Phase VSC

For small-signal stability analysis, a linearized model around an equilibrium point of the power system is required. Many efforts have been made to present a proper small-signal model of a grid-connected VSC in [8,11,15]. The small-signal model of the studied model used in the following assessment is presented in Appendix A. Additionally, the control and system parameters are also provided in Table 2.

Table 2. System and control parameters of the main power system.

Power System Parameters		Control Parameters	
Nominal power (P_n)	10 [kW]	CC	
Nominal line voltage (v_g)	400 [V]	k_{pc}, k_{ic}	9.425, 4.4×10^3
Grid frequency (ω)	50 [Hz]	DVC	
Inverter-side inductor (L_f)	2 [mH]	k_{pd}, k_{id}	0.088, 1.934
Grid-side inductor (L_{g1})	0.5 [mH]	AVC	
Filter capacitor (C_f)	10 [µF]	k_{pa}, k_{ia}	0, 3.428
Grid inductor (L_{g2})	5–30 [mH]	HPF	
Grid SCR	1.67–10	k_a, ω_a	1, 6.6×10^3
DC-link capacitor (C_{dc})	1.5 [mF]	SRF-PLL	
DC-link voltage (v_{dc})	700 [V]	$V_{fd}, \xi_{PLL}, \omega_{PLL}$	400, 0.7, 14π
Sampling and switching frequencies	10 [kHz]	$k_{pp} = \xi_{PLL}.\omega_{PLL}.{V_{fd}}^{-1}$	0.154
T_d	150 [µs]	$k_{ip} = {\omega_{PLL}}^2.{V_{fd}}^{-1}$	4.836

3.2. Operating Point Calculation of the Grid-Connected Three-Phase VSC

The obtained linearized state–space model needed steady-state values for the PCC voltage and current. These could be obtained by evaluating the nonlinear state–space model or conducting simulations, which were more accurate but more time-consuming. This subsection presents a simple algorithm to calculate the operating point condition based on the mathematical model and Figure 5, as shown in (3).

$$\begin{aligned}
&Inputs \rightarrow P, C_f, L_{g1}, L_{g2}, V_{dc}, V_{fd}, V_g \\
&X_g = \omega_1(L_{g1} + L_{g2}), X_C = \tfrac{1}{C_f \omega_1}, \delta = a\sin\left(\tfrac{X_g.P}{V_{fd}V_g}\right), \\
&Q_g = \tfrac{V_g}{X_g}\left(V_{fd}\cos(\delta) - V_g\right), S_g = \sqrt{{Q_g}^2 + P^2}, |I_g| = \tfrac{S_g}{V_{fd}} \\
&Q_L = X_g.|I_g|^2, Q_C = \tfrac{{V_{fd}}^2}{X_C}, Q_{inv} = Q_g + Q_L - Q_C \\
&I_{dc} = \tfrac{P}{V_{dc}}, I_{fd} = \tfrac{P}{V_{fd}}, I_{fq} = \tfrac{-Q_{inv}}{V_{fd}} \\
&Outputs \rightarrow I_{dc}, I_{fd}, I_{fq}
\end{aligned} \tag{3}$$

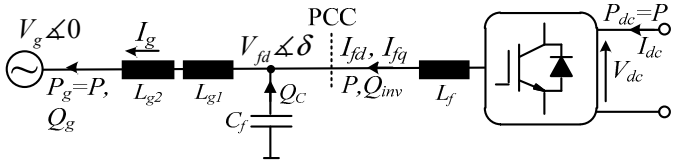

Figure 5. Power flow diagram in a grid-connected VSC.

In summary, the inverter power level and grid inductance (P, L_{g2}) were two independent inputs that impacted the VSC operating point. Moreover, it was assumed that the system was stable and, hence, the control system could keep the DC-link voltage (V_{dc}) and AC magnitude of the PCC voltage (V_{fd}) at the desired values (here, V_{dc} = 700 V, V_{fd} = 400 V). Therefore, based on the mentioned parameters and assumptions, the PCC (I_{fd}, I_{fq}) and DC source (I_{dc}) currents could be calculated. All parameters and signals were available to build the state–space model of the system (A1).

4. Results of Probabilistic Stability and Performance Assessment

This section evaluates the impact of uncertainties in grid SCR and operating point conditions and different PLL bandwidths on the system stability and performance through the proposed probabilistic methodology. It is worth remarking that although many research works considered these uncertainties, this section tried to present a new probabilistic point of view and widen the available knowledge. The proposed methodology measured the system stability and performance, not only by the absolute values of the stability indices (based on the deterministic assessment) but also in terms of their statistical properties (based on the proposed probabilistic assessment). Therefore, the probabilistic evaluation presented in this paper reflected the system behavior better under uncertainties than the conventional one. Moreover, it could provide the likelihood of a specific condition and related the system stability analysis to the risk and reliability assessment.

4.1. The Grid SCR Impact on System Stability and Performance

4.1.1. Critical Mode Locus in the S-Plan

This subsection investigates the impact of grid SCR variations on the system stability and performance. In this respect, five different levels for grid SCR (10, 5, 2.5, 2, and 1.67) were considered and a proper normal PDF was defined for each of them, or equivalently for grid inductances in Figure 6a.

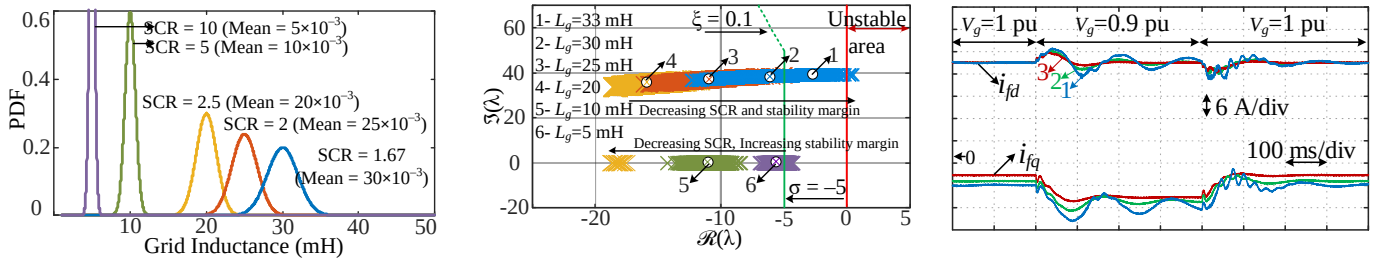

(**a**) (**b**) (**c**)

Figure 6. Probabilistic assessment and transient response of a grid-connected VSC. (**a**) Probability density functions (PDFs) of a normal distribution considering different levels of grid SCR; (**b**) critical mode locations in the complex s-plane due to considered uncertainties; (**c**) time-domain simulations showing inverter current under 10% voltage sag at grid voltage and different grid SCRs ($P = P_n$); numbers indicate the operation under different grid SCRs, i.e., 1, 2, and 3 represent grid SCR equal to 1.51, 1.67, and 2, respectively.

The mean values were equal to each SCR level, and the standard deviation was equal to 6.67% of the mean value. Therefore, the sampled grid SCR and corresponding inductance had a 99.9% confidence of being within ±20%.

It is worth mentioning that a strong grid was introduced when SCR = 5 and 10, 2 < SCR < 3 represented a weak grid, and SCR < 2 corresponded to a very weak grid [11]; therefore, the following analysis could cover a wide range of probable operating conditions of a power system. Figure 6b depicts variations in the system critical mode under different grid conditions.

Before explaining the obtained results, it is worth remarking that the critical mode was computed based on the proposed framework in Figure 1. In such a way, at first, the

Monte Carlo sampling method drew a random grid inductance value from the PDFs of grid inductances (defined in Figure 6a). The sampled grid inductance, the inverter power level, and other fixed control and power system parameters were then used to calculate the steady-state operating point in (3). This information built the stability model up in (A1). Eigenvalue analysis then estimated the critical mode. This procedure was repeated N_C times, and the results were plotted and are shown in Figure 6b. Additionally, the statical properties of the critical mode and corresponding PDFs and CDFs could also be assessed for this case and other inverter powers and PLL bandwidths, which the following subsections discuss.

As shown in Figure 6b, under a weaker grid, the potential locations of the critical modes covered a larger area, meaning there was a higher sensitivity to grid inductance variations.

Moreover, when the SCR decreased from 10 to 2.5 and then from 2.5 to 1.67, two opposite behaviors could be seen. In the first part, the system damping increased, while by further SCR reduction, the stability margin decreased. The main reasons behind this phenomenon could be explained as follows.

As discussed in [40], a VSC with an inverter-side current control has a smaller stability margin under higher SCR; therefore, by reducing the SCR from 10 to 2.5, the system stability margin increased. However, a further SCR reduction resulted in higher grid coupling and control-loop interactions due to PLL and higher grid inductances, which could degrade the system stability and even cause instability.

In addition to this, the AVC could also significantly impact the damping factor in higher SCRs due to its lower bandwidth among different control loops. In this situation, the worst damping factor could be approximated as $\sigma_{\max} = -\omega_{B,AVC}$. For the studied system, the AVC bandwidth changed from 5.38 rad/s (0.85 Hz) to 32.31 rad/s (5.14 Hz), according to $\omega_{B,AVC} = k_{ia}.\omega_1.L_g$ [41]. Therefore, a higher SCR (SCR : 2.5 $\rightarrow$ 10) resulted in a lower AVC bandwidth and, consequently, a smaller damping factor ($\sigma_{\max} = -\omega_{B,AVC} : -21 \rightarrow -5.1$), which can also be seen from Figure 6b. It is worth emphasizing that for a much lower SCR (e.g., SCR < 2.5), since the AVC bandwidth increased and became closer to other control-loop bandwidths, the above conclusions could not be entirely applied to them. In summary, the inverter-side current controller and AVC could impact the stability margins in higher SCRs. In addition, grid coupling and control-loop interactions due to PLL and higher grid inductors were the main reasons for damping reductions at lower SCRs. This discussion is verified by participation factor analysis in Table 3 for a system working under nominal power.

Table 3. Participation factor analysis of critical modes for different grid SCRs and power levels.

SCR	10	5	2.5	2	1.67
$P = 0.05P_n$					
Damping Factor	AVC (0.99)	AVC (0.99)	AVC (0.92)	AVC (0.8), DVC (0.13)	CC (0.46), i_{gdq} (0.23), PLL (0.07), AVC (0.06), APB (0.09)
Damping Ratio	HPF (0.3), Delay (0.27), i_{dq} (0.17), v_{cdq} (0.13)	HPF (33), Delay(0.22), i_{dq} (0.21), v_{cdq} (0.13)	HPF (0.33), Delay (0.22), i_{dq} (0.21), v_{cdq} (0.13)	CC (0.47), i_{gdq} (0.25), PLL (0.06), AVC (0.05), APB (0.08)	CC (0.46), i_{gdq} (0.23), PLL (0.07), AVC (0.06), APB (0.09)
$P = 0.25P_n$					
Damping Factor	AVC (0.99)	AVC (0.99)	AVC (0.92)	AVC (0.73), DVC (0.18)	CC (0.46), i_{gdq} (0.23), PLL (0.08), AVC (0.06), APB (0.08)
Damping Ratio	HPF (31), Delay (0.26), i_{dq} (0.17), v_{cdq} (0.14)	HPF (34), Delay (0.21), i_{dq} (0.22), v_{cdq} (0.13)	HPF (34), Delay (0.2), i_{dq} (0.25), v_{cdq} (0.13)	CC (0.46), i_{gdq} (0.25), PLL (0.06), AVC (0.05), APB (0.08)	CC (0.46), i_{gdq} (0.23), PLL (0.08), AVC (0.06), APB (0.08)

Table 3. *Cont.*

SCR	10	5	2.5	2	1.67
			$P = 0.5P_n$		
Damping Factor	AVC (0.99)	AVC (0.97)	DVC (0.1), AVC (0.87)	PLL (0.56), AVC (0.07), DVC (0.13), APB (0.22)	CC (0.46), i_{gdq} (0.23), PLL (0.08), AVC (0.06), APB (0.08)
Damping Ratio	HPF (31), Delay (0.27), i_{dq} (0.16), v_{cdq} (0.13)	HPF (33), Delay (0.22), i_{dq} (0.2), v_{cdq} (0.13)	HPF (34), Delay (0.2), i_{dq} (0.24), v_{cdq} (0.13)	CC (0.45), i_{gdq} (0.24), PLL (0.1), AVC (0.05), APB (0.07)	CC (0.46), i_{gdq} (0.23), PLL (0.08), AVC (0.06), APB (0.08)
			$P = 0.75P_n$		
Damping Factor	AVC (0.99)	AVC (0.97)	PLL (0.44), AVC (0.08), DVC (0.17), APB (0.21)	PLL (0.42), AVC (0.12), DVC (0.16), APB (0.21)	PLL (0.4), AVC (0.15), DVC (0.15), APB (0.21)
Damping Ratio	HPF (31), Delay (0.27), i_{dq} (0.17), v_{cdq} (0.14)	HPF (33), Delay (0.23), i_{dq} (0.2), v_{cdq} (0.14)	HPF (35), Delay (0.2), i_{dq} (0.24), v_{cdq} (0.14)	CC (0.46), i_{gdq} (0.24), PLL (0.08), AVC (0.05), APB (0.07)	CC (0.46), i_{gdq} (0.23), PLL (0.2), AVC (0.06), APB (0.08)
			$P = P_n$		
Damping Factor	AVC (0.99)	AVC (0.97)	PLL (0.37), AVC (0.13), DVC (0.18), APB (0.23)	PLL (0.35), AVC (0.16), DVC (0.16), APB (0.22)	PLL (0.33), AVC (0.2), DVC (0.14), APB (0.21)
Damping Ratio	HPF (31), Delay (0.27), i_{dq} (0.2), v_{cdq} (0.14)	HPF (33), Delay (0.22), i_{dq} (0.22), v_{cdq} (0.14)	HPF (33), Delay (0.22), i_{dq} (0.22), v_{cdq} (0.14)	CC (0.45), i_{gdq} (0.24), PLL (0.1), AVC (0.05), APB (0.07)	CC (0.45), i_{gdq} (0.24), PLL (0.1), AVC (0.06), APB (0.08)

4.1.2. Nominal and Robust Stability and Performance Comparison

The system's stability and performance under different grid conditions could also be compared in terms of *NS*, *RS*, *NP*, and *RP*. In Figure 6b, the lines show critical mode variations under grid inductance uncertainties, and white circles with colored multiplication signs show the critical mode location under nominal conditions. As an example, the following conclusion could be drawn for SCR = 10 (the purple curve): the critical mode under the nominal condition was in the LHP and met the performance requirements (the green line); hence, the system had nominal stability and performance.

Under grid inductance variations, although the purple lines were in the LHP, they crossed the green line. Therefore, the system was robustly stable, but it did not meet the robust performance definition. In the same manner, conclusions could be drawn for other SCRs that are summarized in Table 4.

Table 4. Nominal and robust stability and performance comparison for different grid SCRs ($P = P_n$).

	SCR				
Indexes	10	5	2.5	2	1.67
Nominal stability (NS)	+	+	+	+	+
Nominal performance (NP)	+	+	+	+	+
Robust performance (RS)	+	+	+	+	−
Robust stability (RP)	−	+	+	+	−

+: criteria fulfilled; −: criteria not fulfilled.

4.1.3. Time-Domain Simulations

Time-domain simulations based on a switching model were also been conducted to validate the previous analytical results. Figure 6c shows results for an inverter current under a 10% voltage sag at grid voltage in three different cases.

In the third case, the critical mode met the stability and performance requirements and was far from the unstable area. The inverter current had a good transient response with low overshoot and oscillations. In the second case, the critical mode moved to the right, but the stability and performance criteria were still met; as expected, the oscillations grew.

In the first case, the system was still stable but very close to an unstable area; therefore, the oscillations increased dramatically, and there was a high overshoot in the outputs.

4.1.4. Critical Mode Statistical Representation

In addition to the previous results, probabilistic assessment could also provide a wealth of statistical information on the desired indices. In Figure 7, PDFs and cumulative density functions (CDFs) of the maximum damping factor and minimum damping ratio for different grid conditions were calculated and plotted. As can be seen, under a lower grid SCR, the PDFs of the damping factor became wider and moved to the RHP, which indicated a higher sensitivity to grid inductance variations and lower stability margins. The same conclusions as the previous subsections could be drawn for the damping factor and ratio changes under different grid SCRs. It could also be concluded that the maximum damping factor was generally related to the slower dynamics of the outer control loops. In contrast, the minimum damping ratio was highly related to faster internal control-loop dynamics, as could be concluded from participation factor analysis and Table 3.

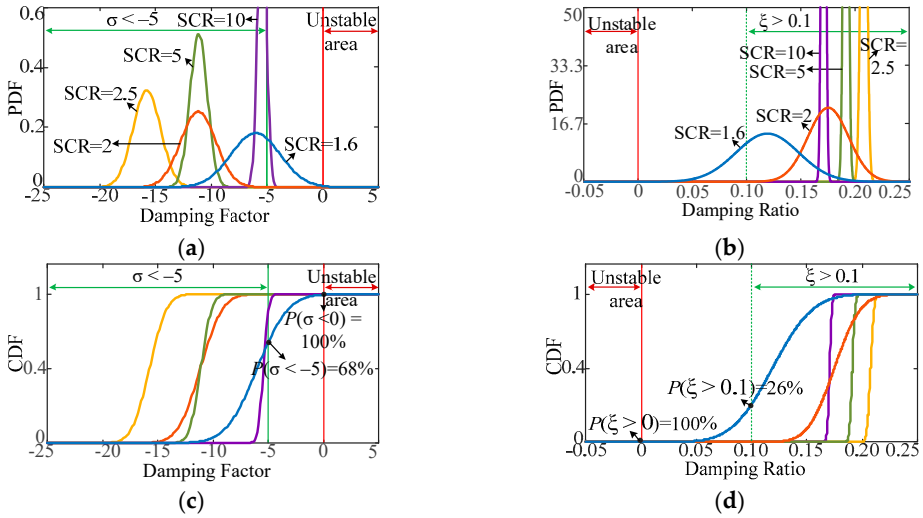

Figure 7. Probability density functions (PDFs) and cumulative density functions (CDFs) of stability indices for different grid SCRs. (**a**,**c**) are PDFs and CDFs of the maximum damping factor; (**b**,**d**) are PDFs and CDFs of the minimum damping ratio. Colors correspond to different grid SCRs in Figure 6a.

Furthermore, CDFs can also provide valuable information on the probability of system stability or the occurrence of desired conditions. They can relate stability analysis to the risk and reliability assessment. In this regard, the risk index of small-signal stability (RIS) is defined as the probability of a damping factor greater than zero $P(\sigma \geq 0)$. From Figure 7c, $P(\sigma < 0)$ is 100%, meaning RIS is zero under all grid SCRs and the system was always stable. In addition, as another example, the likelihood of the desired damping factor $(\sigma < -5)$ for SCR = 1.6 was 68%, and for others it was 100%.

Therefore, the probabilistic assessment could provide the likelihood of a specific condition. In contrast, the deterministic evaluation could not determine how stable a system was or the possibility of system instability. Deterministic methods are treated as binary, i.e., a particular situation is either stable or unstable.

4.2. Inverter Power Level Impact on System Stability and Performance

The inverter power level may affect a system's stability. Therefore, it seemed necessary to investigate this issue. Five different levels for inverter power in the probabilistic assessment were considered. Based on the prepared flow diagram, PDFs of the maximum damping factor and minimum damping ratio were calculated and are shown in Figure 8.

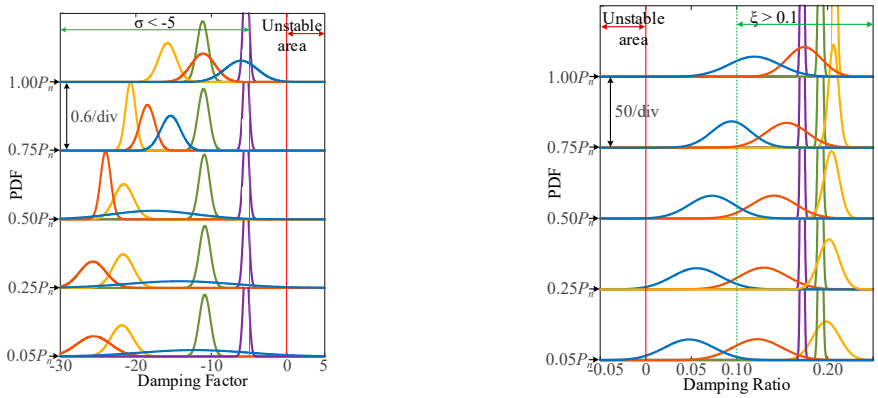

Figure 8. Probability density functions (PDFs) of stability indices for different grid SCRs and power levels. (**a**) PDFs of the maximum damping factor; (**b**) PDFs of the minimum damping ratio. Colors correspond to different grid SCRs in Figure 6a.

4.2.1. Damping Factor Analysis

Two different behaviors for solid and weak grids can be seen from Figure 8a. The damping factor was not affected by the inverter power level in the strong grid. In contrast, it was highly influenced by the power level in the weak grids. As discussed in the previous subsection and as verified by participation factor analysis in Table 3, for the strong grids (higher SCRs), the critical mode was initiated by an AVC due to its lower bandwidth among different control loops. Moreover, grid currents and other control loops did not have much impact. However, under weak grids (lower SCRs), the inner current controller (CC) and outer control loops (PLL, DVC, AVC, and active power balance (APB)) affected the damping of the critical mode at lower and higher output powers, respectively.

4.2.2. Damping Ratio Analysis

As shown in Figure 8b, the grid inductance uncertainties significantly affected the damping ratio in the weak grid and had the least affect in the solid one. For the weak grids, the minimum damping ratio was highly influenced by the fast current control loop (CC). Therefore, by increasing the inverter power level, the SCR that was seen by the current controller under the same grid inductance reduced; thus, the damping ratio improved. The fast dynamic parts, such as the highpass filter (HPF) and control system delay, also contributed to the minimum damping ratio for the strong grids.

4.2.3. Time-Domain Simulations

Time-domain simulations were also prepared to validate the above discussions. Two different SCRs were considered, and the system stability and performance were studied under a grid voltage sag. The PCC voltage under a 10% grid voltage sag and two different power levels are depicted in Figure 9.

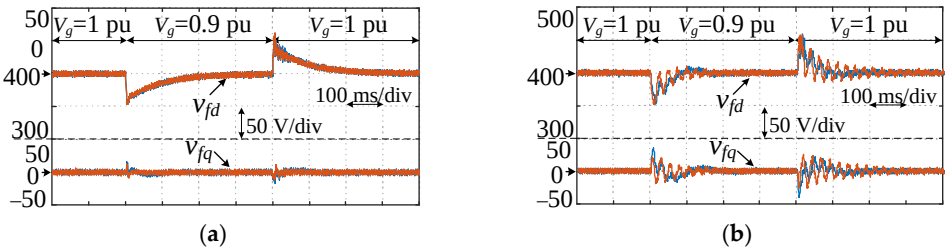

Figure 9. Time-domain simulations showing the system response for 10% voltage sag at grid voltage under different power levels ($P = 0.25P_n$ (orange) and $P = 0.75P_n$, (blue)). (**a**) SCR = 5; (**b**) SCR = 1.67.

As expected due to the analytical results, the system response was the same under different power levels at higher SCRs. However, under lower SCRs, the system response was affected by the inverter power level such that under a lower power level, higher oscillations existed.

4.3. The Impact of PLL Bandwidth on System Stability and Performance

This section investigates the impact of PLL bandwidth on system stability and performance. It is worth remarking that the PLL bandwidth is usually a known and constant parameter, unlike the grid SCR and operating point conditions; hence, the stability assessment could be performed for the provided value of the PLL bandwidth, as presented in Sections 4.1 and 4.2 and as shown in Figures 6–9.

However, additional functionalities were recently suggested for VSCs to support power grids, e.g., transient stability enhancement, virtual inertia implementation, and fault ride-through capability. To fulfil these objectives, a VSC might be equipped with a PLL designed with adaptive or gain scheduling techniques. In this respect, this subsection considers five different values for PLL bandwidth, and the probabilistic assessment is carried out on each of them. The results are presented in Figure 10. This also revealed the importance of an optimal and robust control system design in order to guarantee a stable operation over grid uncertainties. In this regard, the next research step would be a probabilistic control system design that minimizes the probability of the critical mode in the unsuitable area and considers the statistical properties of stability indices. This is highlighted in Section 6 as future work.

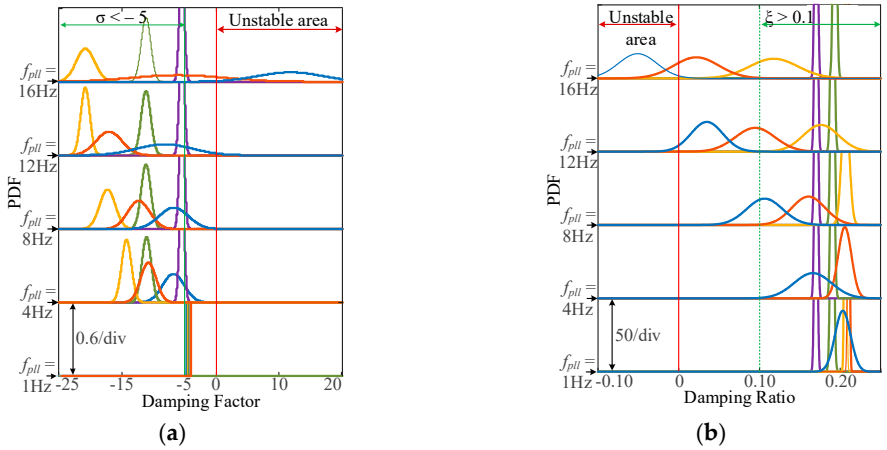

Figure 10. Probability density functions (PDFs) of stability indices for different grid SCRs and PLL bandwidths. (**a**) PDFs of the maximum damping factor; (**b**) PDFs of the minimum damping ratio. Colors correspond to different grid SCRs in Figure 6a. Colors correspond to different grid SCRs in Figure 6a.

4.3.1. Damping Factor Analysis

As shown in Figure 10a and Table 5, for f_{PLL} = 1 Hz, PDFs become very narrow, and it could be concluded that the damping factor was less sensitive to grid inductance variations. However, the stability margin was also insufficient. It could also be deduced from participation factor analysis that the PLL remarkably contributed to the critical mode. In addition, it seemed that the maximum damping factor for lower PLL bandwidths could be estimated by $\sigma_{\max} = -\omega_{B,PLL} = -2\pi f_{PLL}$.

Table 5. Participation factor analysis of critical modes for different grid SCR and PLL bandwidths ($P = P_n$).

SCR	10	5	2.5	2	1.67
f_{PLL} = 1 Hz					
Damping Factor	PLL (0.99)	PLL (0.99)	PLL (0.97)	PLL (0.94)	PLL (0.92)
Damping Ratio	HPF (0.31), Delay (0.27), i_{dq} (0.16), v_{cdq} (0.14)	HPF (33), Delay (0.22), i_{dq} (0.22), v_{cdq} (0.14)	HPF (0.34), Delay (0.21), i_{dq} (0.24), v_{cdq} (0.14)	HPF (0.34), Delay (0.2), i_{dq} (0.25), v_{cdq} (0.13)	CC (0.52), i_{gdq} (0.23), PLL (0.02), AVC (0.06), APB (0.09)
f_{PLL} = 4 Hz					
Damping Factor	AVC (0.99)	AVC (0.96)	PLL (0.5), DVC (0.16), AVC (0.14), ABP (0.14)	PLL (0.42), DVC (0.16), AVC (0.18), ABP (0.16)	PLL (0.38), DVC (0.14), AVC (0.21), ABP (0.17)
Damping Ratio	HPF (0.3), Delay (0.27), i_{dq} (0.16), v_{cdq} (0.14)	HPF (33), Delay (0.23), i_{dq} (0.21), v_{cdq} (0.14)	HPF (34), Delay (0.2), i_{dq} (0.24), v_{cdq} (0.14)	HPF (34), Delay (0.2), i_{dq} (0.25), v_{cdq} (0.14)	CC (0.48), i_{gdq} (0.22), PLL (0.05), AVC (0.06), APB (0.09)
f_{PLL} = 8 Hz					
Damping Factor	AVC (0.99)	AVC (0.96)	PLL (0.34), DVC (0.2), AVC (0.11), APB (0.26)	PLL (0.33), AVC (0.19), DVC (0.17), APB (0.24)	PLL (0.31), DVC (0.14), AVC (0.19), APB (0.23)
Damping Ratio	HPF (31), Delay (0.27), i_{dq} (0.17), v_{cdq} (0.14)	HPF (34), Delay (0.23), i_{dq}(0.2), v_{cdq} (0.14)	HPF (34), Delay (0.2), i_{dq} (0.25), v_{cdq} (0.14)	CC (0.45), i_{gdq} (0.24), PLL (0.1), AVC (0.05), APB (0.07)	CC (0.43), i_{gdq} (0.23), PLL (0.1), AVC (0.06), APB (0.08)
f_{PLL} = 12 Hz					
Damping Factor	AVC (0.99)	AVC (0.96)	PLL (0.01), DVC (0.25), AVC (0.71), APB (0.01),	PLL (0.19), DVC (0.22), AVC (0.15), APB (0.32),	CC (0.38), i_{gdq} (0.2), PLL (0.16), AVC (0.06), APB (0.07),
Damping Ratio	HPF (31), Delay (0.27), i_{dq} (0.17), v_{cdq} (0.14)	HPF (33), Delay (0.22), i_{dq} (0.21), v_{cdq} (0.14)	CC (0.42), i_{gdq} (0.26), PLL (0.12), AVC (0.05), APB (0.07)	CC (0.4), i_{gdq} (0.25), PLL (0.14), AVC (0.05), APB (0.07)	CC (0.38), i_{gdq} (0.24), PLL (0.15), AVC (0.06), APB (0.08)
f_{PLL} = 16 Hz					
Damping Factor	AVC (0.99)	AVC (0.97)	PLL (0.37), APB (0.23), DVC (0.18), AVC (0.13)	PLL (0.35), APB (0.22), DVC (0.16), AVC (0.16)	PLL (0.33), APB (0.21), AVC (0.2), DVC (0.14)
Damping Ratio	HPF (31), Delay (0.26), i_{dq} (0.16), v_{cdq} (0.14)	HPF (33), Delay (0.22), i_{dq} (0.22), v_{cdq} (0.14)	CC (0.38), i_{gdq} (0.26), PLL (0.19), AVC (0.03), APB (0.05)	CC (0.35), i_{gdq} (0.26), PLL (0.21), AVC (0.05), APB (0.06)	CC (0.32), i_{gdq} (0.25), PLL (0.24), AVC (0.06), APB (0.07)

Therefore, it could be expected that the damping factor could be improved by increasing the PLL bandwidth. By increasing the PLL bandwidth to 8 Hz, the stability margin was improved; however, the PDFs became wider, which meant more sensitivity to grid inductance variations and higher coupling and control-loop interactions. Finally, increasing the PLL bandwidth further under weak grid conditions might cause stability problems.

4.3.2. Damping Ratio Analysis

Based on Figure 10b and Table 5, PLL bandwidth had the most considerable effect on the damping ratio in the weak grid and the least effect in the strong one. In the weak grids, for lower and higher PLL bandwidths, fast (CC, HPF, delay) and slow (PLL, DVC, AVC) dynamics of the VSC had the highest contributions to damping ratio, respectively. Furthermore, for higher PLL bandwidths, PDFs became broader, and the critical mode moved to the unstable area.

4.3.3. Time-Domain Simulations

In the first test, the system response for a 20-degree phase jump at grid voltage under different PLL bandwidths was investigated. As can be concluded from Figure 11, very low PLL bandwidths provided a lower amount of oscillations in the inverter current at the cost of a slower dynamic response; it took a long time to reach a steady-state value. On the

other hand, higher PLL bandwidths provided a fast transient response at the price of higher output oscillations. Therefore, the PLL bandwidth selection is a compromise between quick dynamic response, output fluctuations, and system stability.

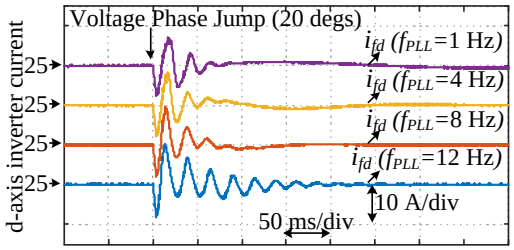

Figure 11. Time-domain simulations showing the system response for 20-degree phase jumps at grid voltage under different PLL bandwidths ($P = P_n$, SCR = 2).

In the second test, the system response for a 10% voltage sag at grid voltage under different grid inductances was studied and the results are shown in Figure 12. Two distinct values for PLL bandwidth, 1 Hz and 12 Hz, were considered to carry out the mentioned scenario.

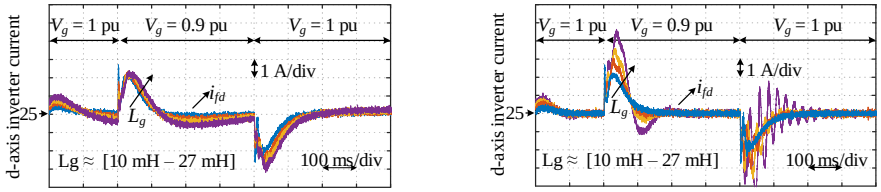

Figure 12. Time-domain simulations showing the system response for 10% voltage sag at grid under grid inductance uncertainties ($P = P_n$), (**a**) f_{PLL} = 1 Hz; (**b**) f_{PLL} =12 Hz.

As expected due to the previous statistical analysis, under lower PLL bandwidths, the system response was not sensitive to grid inductance variations, but the dynamic response was prolonged. In contrast, under higher PLL bandwidths, the dynamic response was relatively faster but it was highly affected by grid inductance variations.

5. Experimental Verification

In this section, experimental tests were carried out to validate the previous analytical results. The experimental setup included two 5 kW Danfoss VSCs operating back-to-back, LCL filters, a grid simulator (Chroma 61845), and a DS1007 dSPACE control system. The first VSC acted as a constant power source, emulating a primary source such as PV or a wind turbine, and supplied the second three-phase grid-connected VSC. The second VSC was connected to a grid simulator through an LCL filter and transfered the received power to the power grid. It contained CC, HPF, PLL, AVC, and DVC. To emulate weak grid conditions and reduce the required inductors in practice, some of the power system and control parameters were changed, and a down-scaled power system was designed. Table 6 shows the parameters that differed from the main circuit parameters.

Table 6. System and control parameters of down-scaled power system.

Power System Parameters		Control Parameters	
Nominal power (P_n)	5 [kW]	Conventional control method	
Nominal line voltage (v_g)	172 [V]	k_{pc}, k_{ic}	7.068, 3.3×10^3
Filter capacitor (C_f)	30 [μF]	k_{pp}, k_{ip}	0.41, 14.7
Inverter-side inductor (L_f)	1.5 [mH]	k_{pa}, k_{ia}	0, 9.23
Grid-side inductor (L_g)	1.9–19 [mH]	Proposed control method	
DC-link voltage (v_{dc})	600 [V]	k_{pp}, k_{ip}	0.41, 14.7

Figures 13 and 14 show the system response under different power levels and PLL bandwidths under weak and strong grid conditions (SCR = 1.63 and 5.3), respectively. Even though a perfect match between the analytical and experiments was not presented due to laboratory implementation limitations, the results demonstrated the same trend.

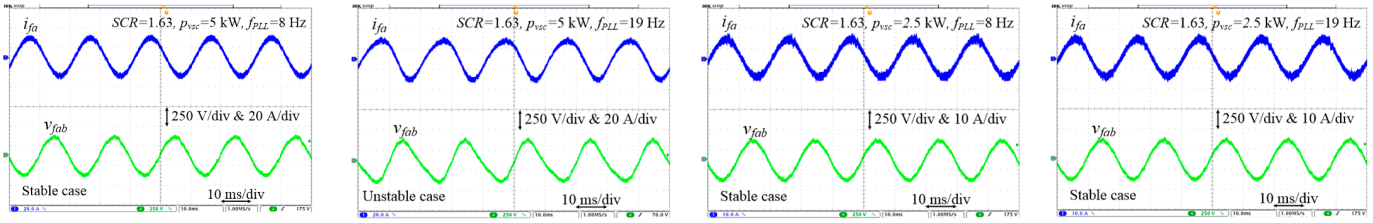

Figure 13. Experimental results showing the system response under weak grid conditions (SCR = 1.63) and different power levels (P = 5 kW, 2.5 kW) and PLL bandwidths (f_{PLL} = 8 Hz, 19 Hz).

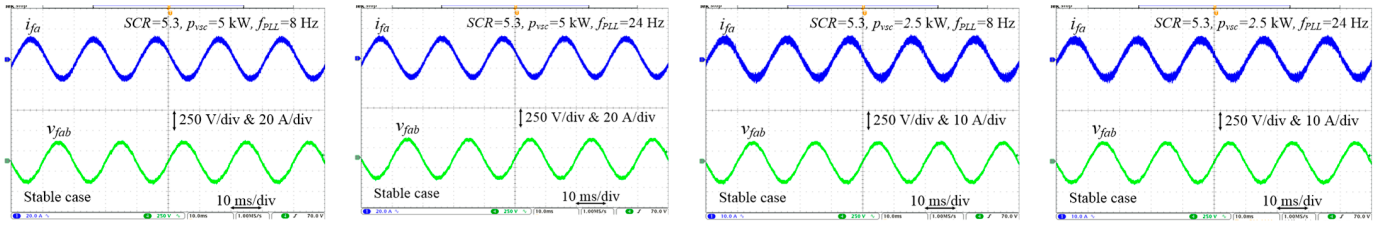

Figure 14. Experimental results showing the system response under strong grid conditions (SCR = 5.3) and different power levels (P = 5 kW, 2.5 kW) and PLL bandwidths (f_{PLL} = 8 Hz, 24 Hz).

As shown, the system response under weak grids was sensitive to inverter power level, and a low grid SCR limited the application of a high-bandwidth PLL. While under a strong grid, this phenomenon could not be seen. The following section summarizes the presented discussions and results in the previous sections.

6. Discussion and Future Works

This work aimed to develop a comprehensive probabilistic framework for the robustness analysis of VSCs for power system applications. From the provided perspective, it was possible to measure system stability and performance using statistical properties of operational indices, which are of utmost importance. Moreover, based on the provided statistical information, the likelihood of a specific condition could be easily calculated, and relationships between the system stability and the risk and reliability assessment were identified. Therefore the proposed framework and defined indices could broaden the existing knowledge on robust stability and performance analysis of VSCs and provide new insights for future works.

To evaluate the applicability of the proposed framework, the impact of uncertainties in the grid SCR, operating point conditions, and control-loop interactions on system stability and the performance of a grid-connected VSC were thoroughly investigated. It is worth remarking that the most crucial stability and performance indicators were the maximum damping factor and minimum damping ratio, which were evaluated for the specified level of plant uncertainty.

It was found that the grid SCR was the most influential parameter on the system stability and performance among the different parameters and could seriously limit the VSC's performance.

Lower Grid SCR results in higher sensitivity of the critical mode to grid inductance variations, which appear in wider PDFs or lower slopes of CDFs. CDFs could also determine the risk of system instability or the likelihood of a particular condition. In contrast, the deterministic methods were only treat as binary.

It was also concluded that the stability and performance of VSCs were not affected by the inverter power level for strong grids. In contrast, the opposite observation was observed for weak grids. Increasing the inverter loading increased the stability margin at first. However, at higher levels, stability margins were again reduced due to higher coupling and interactions between different control parts.

The impact of PLL bandwidth was also investigated with respect to the system stability and performance. Under very low PLL bandwidths, VSCs and power grids could be assumed decoupled due to very narrow PDFs in the outputs. However, the stability margin was also insufficient, which was not desirable. It could be expected that increasing the PLL bandwidth increases the stability margin; however, PDFs could become broader than before, which could increase coupling between the grid and the VSC and increase sensitivity to grid inductance variations. Additionally, system instability might occur for higher PLL bandwidths under weak grid conditions; therefore, low and high PLL bandwidths might reduce the stability margin and drive the system to instability. Consequently, this parameter should be carefully selected.

It is worth noting that for the usual selection of control parameters, fast dynamic parts of the VSC, such as the current controller, highpass filter, control delay, etc., had a significant impact on the minimum damping ratio. Moreover, outer and slow control parts such as AVC, DVC, PLL, etc., influenced the maximum damping factor. For strong grids, AVC usually had a lower bandwidth among the different control loops, and it had a significant impact on the maximum damping factor. For weak grids, the damping factor of the critical mode was more sensitive to PLL bandwidths, and different control-loop interactions influenced it remarkably.

In summary, the proposed probabilistic robustness assessment could achieve the following:

- Reveal the range of the critical mode variations;
- Demonstrate the sensitivity of the critical mode to uncertainty in different system parameters;
- Identify the risk of system instability and the probability of occurrence of a specific condition;
- Identify major parameters contributing to system stability;
- Easily include the stochastic nature of renewables;
- Allow better utilization of existing assets compared to the deterministic approaches based on worst-case scenarios.

For future works, investigating the impacts of outer control loops, such as DVC and AVC, on system stability and performance are also recommended. Additional stability and performance indicators, such as frequency of oscillations, phase and gain margins, steady-state error, disturbance rejections capability, singular values, etc., could be defined and developed to clarify system behavior better. Moreover, robustness analysis considering the mission profiles of PV modules or wind turbine systems, resonances in the grid impedance, and unbalanced network conditions would be interesting. Probabilistic control system design, which minimizes the probability of the critical mode in the unsuitable area, would be an exciting topic as well. Finally, considering more complex and larger power systems is highly recommended. When multiple power electronic converters are connected to the point of common coupling, different behaviors might occur and possible interactions between power converters and passive elements of power systems might adversely affect the entire system operation.

7. Conclusions

This paper proposed a probabilistic framework that could be adopted for robust stability and performance analysis of VSCs for power system applications. It provided the desired statistical information that could better reflect a system's performance under different uncertainties and disturbances.

In addition, it provided the risk of system instability or the likelihood of a specific situation, which is of utmost importance for power system design and utilization.

The proposed probabilistic framework was applied to an LCL-filtered grid-connected VSC to evaluate the applicability of the proposed methodology and broaden the available knowledge on the robustness of VSCs. The obtained results showed that a grid SCR could vigorously limit a system's stability and performance; hence, under the lower grid SCR, PDFs of stability indices became wider and moved to the unstable area, meaning there was a higher sensitivity in the critical mode to grid inductance variations and smaller stability margins. It was also concluded that, although stability and performance were not affected by the inverter power level in a strong grid, it was remarkably affected in a weak grid. In weak grids, the stability margin might not be sufficient under lower inverter power levels. Moreover, it was found that the PLL bandwidth selection was a compromise between the fast dynamic response and stability margin. Lower PLL bandwidths resulted in thinner PDFs, meaning lower coupling between the VSC and grid, but the transient response was slow and the stability margin might not be adequate. Higher PLL bandwidth results in faster transient response and broader PDFs, revealing more coupling between the grid and VSC and higher sensitivity to grid inductance variations. In summary, based on the proposed probabilistic sensitivity assessment, a system's dynamic behavior under different system uncertainties and disturbances was entirely investigated. Moreover, the main phenomena and reasons behind each observation were fully explained.

Author Contributions: Conceptualization, H.G.-K., P.D., M.N. and F.B.; methodology, H.G.-K.; software, H.G.-K.; validation, H.G.-K.; formal analysis, H.G.-K. and P.D.; investigation, H.G.-K., P.D., M.N. and F.B.; resources, P.D. and F.B.; data curation, H.G.-K.; writing—original draft preparation, H.G.-K.; writing—review and editing, H.G.-K., P.D., M.N. and F.B.; visualization, H.G.-K.; supervision, F.B., P.D. and M.N.; project administration, H.G.-K.; funding acquisition, F.B. and P.D. All authors have read and agreed to the published version of the manuscript.

Funding: This work was supported by the Reliable Power Electronic-Based Power System project at AAU Energy, Aalborg University, Aalborg, Denmark, as a part of the Villum Investigator Program funded by the Villum Foundation.

Institutional Review Board Statement: Not applicable.

Informed Consent Statement: Not applicable.

Data Availability Statement: Not applicable.

Conflicts of Interest: The authors declare no conflict of interest.

Appendix A

Small-Signal Modeling of the Grid-Connected Three-Phase VSC

The closed-loop system can be written as follows [8,15]:

$$\dot{x}_{sys} = A_{sys} x_{sys} \tag{A1}$$

Here, x_{sys} and A_{sys} are system states and the closed-loop state matrix (A2) and (A3). In (A2), CC, HPF, delay, PLL, DVC, AVC, and APB (active power balance) refer to different VSC dynamics associated with different power and control parts. Moreover, ${i_{fdq}}^c$, i_{gdq}, and v_{fdq} are inverter and grid currents and the capacitor voltage, respectively. It is worth noting that there are two dq-frames in the system small-signal model to include the PLL dynamics. The converter dq-frame with superscript c, which is aligned by the phase angle obtained by the PLL, and grid dq-frame without superscript aligned by the positive sequence of PCC voltage. In (A3), r_f, r_g, and r_c are the series-equivalent resistances of L_f, L_g and C_f, respectively.

$$x_{sys} = \left[\overbrace{\gamma_{id}, \gamma_{iq}}^{CC}, \overbrace{x_{ffd}, x_{ffq}}^{HPF}, \overbrace{x_{d1}, x_{d2}, x_{d3}, x_{q1}, x_{q2}, x_{q3}}^{Delay}, {i_{fd}}^c, {i_{fq}}^c, \overbrace{\varphi_q, \theta}^{PLL}, \overbrace{\gamma_{dc}}^{DVC}, \overbrace{x_{ac}}^{AVC}, \overbrace{x_{dc}}^{APB}, v_{fd}, i_{gd}, v_{fq}, i_{gq} \right]^T \tag{A2}$$

$$A_{sys} = \begin{bmatrix}
0 & 0 & 0 & 0 & 0 & 0 & 0 & 0 & 0 & 0 & -1-\frac{k_{pd}L_fI_{fd}}{C_{dc}V_{fd}} & -\frac{k_{pd}L_fI_{fq}}{C_{dc}V_{fd}} & 0 & 0 & 1 & 0 & -\frac{k_{pd}V_{dc}}{V_{fd}} & 0 & 0 & 0 & 0 \\
0 & 0 & 0 & 0 & 0 & 0 & 0 & 0 & 0 & 0 & 0 & -1 & 0 & 0 & 0 & 1 & 0 & k_{pa} & 0 & 0 & 0 \\
0 & 0 & $-\omega_a$ & 0 & 0 & 0 & 0 & 0 & 0 & 0 & 0 & 0 & 0 & 0 & 0 & 0 & 0 & 1 & 0 & 0 & 0 \\
0 & 0 & 0 & $-\omega_a$ & 0 & 0 & 0 & 0 & 0 & 0 & 0 & 0 & 0 & $-V_{fd}$ & 0 & 0 & 0 & 0 & 0 & 1 & 0 \\
0 & 0 & 0 & 0 & 0 & 1 & 0 & 0 & 0 & 0 & 0 & 0 & 0 & 0 & 0 & 0 & 0 & 0 & 0 & 0 & 0 \\
0 & 0 & 0 & 0 & 0 & 0 & 1 & 0 & 0 & 0 & 0 & 0 & 0 & 0 & 0 & 0 & 0 & 0 & 0 & 0 & 0 \\
k_{ic} & 0 & $-k_a\omega_a$ & 0 & $\left(\frac{-120}{T_d{}^3}\right)$ & $\left(\frac{-60}{T_d{}^2}\right)$ & $\left(\frac{-12}{T_d}\right)$ & 0 & 0 & 0 & $-k_{pc}\left(1+\frac{k_{pd}L_fI_{fd}}{C_{dc}V_{fd}}\right)$ & $-\frac{k_{pc}k_{pd}L_fI_{fq}}{C_{dc}V_{fd}}$ & 0 & 0 & k_{pc} & 0 & $-\frac{k_{pc}k_{pd}V_{dc}}{V_{fd}}$ & k_a & 0 & 0 & 0 \\
0 & 0 & 0 & 0 & 0 & 0 & 0 & 0 & 1 & 0 & 0 & 0 & 0 & 0 & 0 & 0 & 0 & 0 & 0 & 0 & 0 \\
0 & 0 & 0 & 0 & 0 & 0 & 0 & 0 & 0 & 1 & 0 & 0 & 0 & 0 & 0 & 0 & 0 & 0 & 0 & 0 & 0 \\
0 & k_{ic} & 0 & $-k_a\omega_a$ & 0 & 0 & 0 & $\left(\frac{-120}{T_d{}^3}\right)$ & $\left(\frac{-60}{T_d{}^2}\right)$ & $\left(\frac{-12}{T_d}\right)$ & 0 & $-k_{pc}$ & 0 & $-k_aV_{fd}$ & 0 & k_{pc} & 0 & $k_{pc}k_{pa}$ & 0 & k_a & 0 \\
$\frac{-k_{ic}}{L_f}$ & 0 & $\frac{k_a\omega_a}{L_f}$ & 0 & $\frac{240}{L_fT_d{}^3}$ & 0 & $\frac{24}{L_fT_d}$ & 0 & 0 & 0 & $\left(\frac{-r_f+k_{pc}}{L_f}+\frac{k_{pc}k_{pd}I_{fd}}{C_{dc}V_{fd}}\right)$ & $\left(\omega_1+\frac{k_{pc}k_{pd}I_q}{C_{dc}V_{fd}}\right)$ & 0 & 0 & $-\frac{k_{pc}}{L_f}$ & 0 & $\frac{k_{pc}k_{pd}V_{dc}}{L_fV_{fd}}$ & $\left(\frac{-1-k_a}{L_f}\right)$ & 0 & 0 & 0 \\
0 & $\frac{-k_{ic}}{L_f}$ & 0 & $\frac{k_a\omega_a}{L_f}$ & 0 & 0 & 0 & $\frac{240}{L_fT_d{}^3}$ & 0 & $\frac{24}{L_fT_d}$ & $-\omega_1$ & $\left(\frac{-r_f+k_{pc}}{L_f}\right)$ & 0 & $\frac{(k_a+1)V_{fd}}{L_f}$ & 0 & $\frac{-k_{pc}}{L_f}$ & 0 & $-\frac{k_{pc}k_{pa}}{L_f}$ & 0 & $\frac{-(k_a+1)}{L_f}$ & 0 \\
0 & 0 & 0 & 0 & 0 & 0 & 0 & 0 & 0 & 0 & 0 & 0 & 0 & $-V_{fd}$ & 0 & 0 & 0 & 0 & 0 & 1 & 0 \\
0 & 0 & 0 & 0 & 0 & 0 & 0 & 0 & 0 & 0 & 0 & 0 & k_{ip} & $-k_{pp}V_{fd}$ & 0 & 0 & 0 & 0 & 0 & k_{pp} & 0 \\
0 & 0 & 0 & 0 & 0 & 0 & 0 & 0 & 0 & 0 & $-\frac{k_{id}L_fI_{fd}}{C_{dc}V_{fd}}$ & $-\frac{k_{id}L_fI_{fq}}{C_{dc}V_{fd}}$ & 0 & 0 & 0 & 0 & $-\frac{k_{id}V_{dc}}{V_{fd}}$ & 0 & 0 & 0 & 0 \\
0 & 0 & 0 & 0 & 0 & 0 & 0 & 0 & 0 & 0 & 0 & 0 & 0 & 0 & 0 & 0 & 0 & k_{ia} & 0 & 0 & 0 \\
0 & 0 & 0 & 0 & 0 & 0 & 0 & 0 & 0 & 0 & $\left(\frac{V_{fd}}{C_{dc}V_{dc}}+\frac{L_fI_{dc}I_{fd}}{(C_{dc}V_{dc})^2}\right)$ & $\frac{L_fI_{dc}I_{fq}}{(C_{dc}V_{dc})^2}$ & 0 & $\frac{-V_{fd}I_{fq}}{C_{dc}V_{dc}}$ & 0 & 0 & $\frac{I_{dc}}{C_{dc}V_{dc}}$ & $\frac{I_{fd}}{C_{dc}V_{dc}}$ & 0 & $\frac{I_{fq}}{C_{dc}V_{dc}}$ & 0 \\
0 & 0 & 0 & 0 & 0 & 0 & 0 & 0 & 0 & 0 & $\frac{1}{C_f}$ & 0 & 0 & $\frac{-I_q}{C_f}$ & 0 & 0 & 0 & 0 & $\frac{-1}{C_f}$ & ω_1 & 0 \\
0 & 0 & 0 & 0 & 0 & 0 & 0 & 0 & 0 & 0 & $\frac{r_c}{L_g}$ & 0 & 0 & $\frac{-r_cI_{fq}}{L_g}$ & 0 & 0 & 0 & $\frac{1}{L_g}$ & $\left(\frac{-r_g-r_c}{L_g}\right)$ & 0 & ω_1 \\
0 & 0 & 0 & 0 & 0 & 0 & 0 & 0 & 0 & 0 & 0 & $\frac{1}{C_f}$ & 0 & $\frac{I_{fd}}{C_f}$ & 0 & 0 & 0 & $-\omega_1$ & 0 & 0 & $\frac{-1}{C_f}$ \\
0 & 0 & 0 & 0 & 0 & 0 & 0 & 0 & 0 & 0 & 0 & $\frac{r_c}{L_g}$ & 0 & $\frac{r_cI_{fd}}{L_g}$ & 0 & 0 & 0 & 0 & $-\omega_1$ & $\frac{1}{L_g}$ & $\left(\frac{-r_g-r_c}{L_g}\right)$
\end{bmatrix} \quad \text{(A3)}$$

References

1. International Energy Agency (IEA). *Renewables 2020, Analysis and Forecast to 2025*; Technical Report; IEA: Paris, France, 2020; Available online: https://www.iea.org/reports/renewables-2020 (accessed on 4 July 2022).
2. Farrokhabadi, M.; Lagos, D.; Wies, R.W.; Paolone, M.; Liserre, M.; Meegahapola, L.; Kabalan, M.; Hajimiragha, A.H.; Peralta, D.; Elizondo, M.A.; et al. Microgrid Stability Definitions, Analysis, and Examples. *IEEE Trans. Power Syst.* **2020**, *35*, 13–29. [CrossRef]
3. Ma, R.; Qiu, Q.; Kurths, J.; Zhan, M. Fast-Slow-Scale Interaction Induced Parallel Resonance and Its Suppression in Voltage Source Converters. *IEEE Access* **2021**, *9*, 90126–90141. [CrossRef]
4. Huang, L.; Xin, H.; Li, Z.; Ju, P.; Yuan, H.; Lan, Z.; Wang, Z. Grid-Synchronization Stability Analysis and Loop Shaping for PLL-Based Power Converters with Different Reactive Power Control. *IEEE Trans. Smart Grid* **2020**, *11*, 501–516. [CrossRef]
5. Wang, X.; Blaabjerg, F. Harmonic Stability in Power Electronic-Based Power Systems: Concept, Modeling, and Analysis. *IEEE Trans. Smart Grid* **2019**, *10*, 2858–2870. [CrossRef]
6. Dong, D.; Wen, B.; Boroyevich, D.; Mattavelli, P.; Xue, Y. Analysis of Phase-Locked Loop Low-Frequency Stability in Three-Phase Grid-Connected Power Converters Considering Impedance Interactions. *IEEE Trans. Ind. Electron.* **2015**, *62*, 310–321. [CrossRef]
7. Harnefors, L.; Bongiorno, M.; Lundberg, S. Input-Admittance Calculation and Shaping for Controlled Voltage-Source Converters. *IEEE Trans. Ind. Electron.* **2007**, *54*, 3323–3334. [CrossRef]
8. Yang, D.; Wang, X. Unified Modular State-Space Modeling of Grid-Connected Voltage-Source Converters. *IEEE Trans. Power Electron.* **2020**, *35*, 9700–9715. [CrossRef]
9. Gholami-Khesht, H.; Davari, P.; Blaabjerg, F. Adaptive Predictive-DPC for LCL-Filtered Grid Connected VSC with Reduced Number of Sensors. In Proceedings of the 2020 22nd European Conference on Power Electronics and Applications (EPE'20 ECCE Europe), Lyon, France, 7–11 September 2020; pp. 1–10. [CrossRef]
10. Gholami-Khesht, H.; Davari, P.; Blaabjerg, F. An Adaptive Model Predictive Voltage Control for LC-Filtered Voltage Source Inverters. *Appl. Sci.* **2021**, *11*, 704. [CrossRef]
11. Huang, Y.; Yuan, X.; Hu, J.; Zhou, P. Modeling of VSC Connected to Weak Grid for Stability Analysis of DC-Link Voltage Control. *IEEE J. Emerg. Sel. Top. Power Electron.* **2015**, *3*, 1193–1204. [CrossRef]
12. Egea-Alvarez, A.; Fekriasl, S.; Hassan, F.; Gomis-Bellmunt, O. Advanced Vector Control for Voltage Source Converters Connected to Weak Grids. *IEEE Trans. Power Syst.* **2015**, *30*, 3072–3081. [CrossRef]
13. Xie, Z.; Chen, Y.; Wu, W.; Xu, Y.; Wang, H.; Guo, J.; Luo, A. Modeling and Control Parameters Design for Grid-Connected Inverter System Considering the Effect of PLL and Grid Impedance. *IEEE Access* **2020**, *8*, 40474–40484. [CrossRef]
14. Zhang, C.; Cai, X.; Rygg, A.; Molinas, M. Sequence Domain SISO Equivalent Models of a Grid-Tied Voltage Source Converter System for Small-Signal Stability Analysis. *IEEE Trans. Energy Convers.* **2018**, *33*, 741–749. [CrossRef]
15. Wang, X.; Harnefors, L.; Blaabjerg, F. Unified Impedance Model of Grid-Connected Voltage-Source Converters. *IEEE Trans. Power Electron.* **2018**, *33*, 1775–1787. [CrossRef]
16. Rygg, A.; Molinas, M.; Zhang, C.; Cai, X. A Modified Sequence-Domain Impedance Definition and Its Equivalence to the Dq-Domain Impedance Definition for the Stability Analysis of AC Power Electronic Systems. *IEEE J. Emerg. Sel. Top. Power Electron.* **2016**, *4*, 1383–1396. [CrossRef]
17. Harnefors, L.; Yepes, A.G.; Vidal, A.; Doval-Gandoy, J. Passivity-Based Controller Design of Grid-Connected VSCs for Prevention of Electrical Resonance Instability. *IEEE Trans. Ind. Electron.* **2015**, *62*, 702–710. [CrossRef]
18. Radwan, A.A.A.; Mohamed, Y.A.R.I. Assessment and Mitigation of Interaction Dynamics in Hybrid AC/DC Distribution Generation Systems. *IEEE Trans. Smart Grid* **2012**, *3*, 1382–1393. [CrossRef]
19. Rosso, R.; Cassoli, J.; Buticchi, G.; Engelken, S.; Liserre, M. Robust Stability Analysis of LCL Filter Based Synchronverter under Different Grid Conditions. *IEEE Trans. Power Electron.* **2019**, *34*, 5842–5853. [CrossRef]

20. Sumsurooah, S.; Odavic, M.; Bozhko, S. μ Approach to Robust Stability Domains in the Space of Parametric Uncertainties for a Power System with Ideal CPL. *IEEE Trans. Power Electron.* **2018**, *33*, 833–844. [CrossRef]
21. Sumsurooah, S.; Odavic, M.; Bozhko, S.; Boroyevich, D. Robust Stability Analysis of a DC/DC Buck Converter under Multiple Parametric Uncertainties. *IEEE Trans. Power Electron.* **2018**, *33*, 5426–5441. [CrossRef]
22. Toulabi, M.; Bahrami, S.; Ranjbar, A.M. Application of Edge Theorem for Robust Stability Analysis of a Power System with Participating Wind Power Plants in Automatic Generation Control Task. *IET Renew. Power Gener.* **2017**, *11*, 1049–1057. [CrossRef]
23. Liu, Z.; Su, M.; Sun, Y.; Yuan, W.; Han, H.; Feng, J. Existence and Stability of Equilibrium of DC Microgrid with Constant Power Loads. *IEEE Trans. Power Syst.* **2018**, *33*, 6999–7010. [CrossRef]
24. Liu, J.; Zhang, W.; Rizzoni, G. Robust Stability Analysis of DC Microgrids with Constant Power Loads. *IEEE Trans. Power Syst.* **2018**, *33*, 851–860. [CrossRef]
25. Gholami-Khesht, H.; Davari, P.; Novak, M.; Blaabjerg, F. Robust H∞ Current Control of Three-Phase Grid-Connected Voltage Source Converters Using Linear Matrix Inequalities. In Proceedings of the 2021 IEEE 22nd Workshop on Control and Modelling of Power Electronics (COMPEL), Cartagena, Colombia, 2–5 November 2021; pp. 1–6.
26. Rosso, R.; Buticchi, G.; Liserre, M.; Zou, Z.; Engelken, S. Stability Analysis of Synchronization of Parallel Power Converters. In Proceedings of the IECON 2017—43rd Annual Conference of the IEEE Industrial Electronics Society, Beijing, China, 29 October–1 November 2017; pp. 440–445.
27. Preece, R.; Huang, K.; Milanović, J.V. Probabilistic Small-Disturbance Stability Assessment of Uncertain Power Systems Using Efficient Estimation Methods. *IEEE Trans. Power Syst.* **2014**, *29*, 2509–2517. [CrossRef]
28. Munikoti, S.; Natarajan, B.; Jhala, K.; Lai, K. Probabilistic Voltage Sensitivity Analysis to Quantify Impact of High PV Penetration on Unbalanced Distribution System. *IEEE Trans. Power Syst.* **2021**, *36*, 3080–3092. [CrossRef]
29. De Souza De Oliveira, D.; Jorge Araujo De Souza, M.; Borges Leal, G.C.; Andrade Leite Alves, F.; Aredes, M. Probabilistic Assessment of the VSC-HVDC Contribution in Voltage Stability Applied to a Hybrid DC-Multi-Infeed Scenario. In Proceedings of the IECON 2020 The 46th Annual Conference of the IEEE Industrial Electronics Society, Singapore, 18–21 October 2020; pp. 1684–1691. [CrossRef]
30. Wang, P.; Zhang, Z.; Huang, Q.; Lee, W.J. Wind Farm Dynamic Equivalent Modeling Method for Power System Probabilistic Stability Assessment. *IEEE Trans. Ind. Appl.* **2020**, *56*, 2273–2280. [CrossRef]
31. Papadopoulos, P.N.; Milanović, J.V. Probabilistic Framework for Transient Stability Assessment of Power Systems with High Penetration of Renewable Generation. *IEEE Trans. Power Syst.* **2017**, *32*, 3078–3088. [CrossRef]
32. He, P.; Chen, J.; Wu, X.; Qi, P.; Shen, R.; Yin, W. Probabilistic Small Signal Stability Assessment of Large-Scale Wind Power Integration. In Proceedings of the 2019 IEEE Innovative Smart Grid Technologies—Asia (ISGT Asia), Chengdu, China, 21–24 May 2019; pp. 1248–1253. [CrossRef]
33. Mochamad, R.F.; Ehsan, A.; Preece, R. Probabilistic Multi-Stability Assessment in Power Systems with Uncertain Wind Generation. In Proceedings of the 2020 International Conference on Probabilistic Methods Applied to Power Systems (PMAPS), Liege, Belgium, 18–21 August 2020; pp. 18–23. [CrossRef]
34. Khodabakhshian, A.; Hemmati, R. Multi-Machine Power System Stabilizer Design by Using Cultural Algorithms. *Int. J. Electr. Power Energy Syst.* **2013**, *44*, 571–580. [CrossRef]
35. Peyghami, S.; Palensky, P.; Blaabjerg, F. An Overview on the Reliability of Modern Power Electronic Based Power Systems. *IEEE Open J. Power Electron.* **2020**, *1*, 34–50. [CrossRef]
36. Coroiu, F.; Velicescu, C.; Barbulescu, C. Probabilistic and Deterministic Load Flows Methods in Power Systems Reliability Estimation. In Proceedings of the 2011 IEEE EUROCON—International Conference on Computer as a Tool, Lisbon, Portugal, 27–29 April 2011; pp. 2–5. [CrossRef]
37. Coroiu, F.; Dondera, D.; Velicescu, C.; Vuc, G. Power Systems Reliability Evaluation Using Probabilistic Load Flows Methods. In Proceedings of the 45th International Universities Power Engineering Conference UPEC2010, Cardiff, UK, 31 August–3 September 2010; pp. 1–5.
38. Sangwongwanich, A.; Yang, Y.; Sera, D.; Blaabjerg, F. Lifetime Evaluation of Grid-Connected PV Inverters Considering Panel Degradation Rates and Installation Sites. *IEEE Trans. Power Electron.* **2018**, *33*, 1225–1236. [CrossRef]
39. Jedtberg, H.; Pigazo, A.; Liserre, M.; Buticchi, G. Analysis of the Robustness of Transformerless PV Inverter Topologies to the Choice of Power Devices. *IEEE Trans. Power Electron.* **2017**, *32*, 5248–5257. [CrossRef]
40. Wang, J.; Yan, J.D.; Jiang, L.; Zou, J. Delay-Dependent Stability of Single-Loop Controlled Grid-Connected Inverters with LCL Filters. *IEEE Trans. Power Electron.* **2016**, *31*, 743–757. [CrossRef]
41. Zhang, H.; Harnefors, L.; Wang, X.; Hasler, J.-P.; Ostlund, S.; Danielsson, C.; Gong, H. Loop-at-a-Time Stability Analysis for Grid-Connected Voltage-Source Converters. *IEEE J. Emerg. Sel. Top. Power Electron.* **2021**, *9*, 5807–5821. [CrossRef]